

Instabilities of captured shocks in the envelopes of massive stars

M. Grott^{1?}, W. Glatzel¹ and S. Chemigovski²

¹Universitäts-Sternwarte Göttingen, Geismarlandstraße 11, D-37083 Göttingen, Germany

²Institut für Analysis und Numerik, Universität Magdeburg, Universitätsplatz 2, D-39106 Magdeburg, Germany

11 April 2024

ABSTRACT

The evolution of strange mode instabilities into the non linear regime has been followed by numerical simulation for an envelope model of a massive star having solar chemical composition, $M = 50 M_{\odot}$, $T_e = 10^4 K$ and $L = 1.17 \cdot 10^6 L_{\odot}$. Contrary to previously studied models, for these parameters shocks are captured in the H-ionisation zone and perform rapid oscillations within the latter. A linear stability analysis is performed to verify that this behaviour is physical. The origin of an instability discovered in this way is identified by construction of an analytical model. As a result, the stratification turns out to be essential for instability. The difference to common stratification instabilities, e.g., convective instabilities, is discussed.

Key words: hydrodynamics – instabilities – shock waves – stars: mass-loss – stars: oscillations – stars: variables: other.

1 INTRODUCTION

Massive stars are known to suffer from strange mode instabilities with growth rates in the dynamical range (Kiriakidis, Fricke & Glatzel 1993; Glatzel & Kiriakidis 1993). The boundary of the domain in the Hertzsprung-Russell diagram (HRD) where all stellar models are unstable – irrespective of their metallicity Z , coincides with the observed Humphreys-Davidson (HD) limit (Humphreys & Davidson 1979). Moreover, the range of unstable models covers the stellar parameters for which the LBV (luminous blue variable) phenomenon is observed.

The high growth rates of the instabilities indicate a connection to the observed mass loss of the corresponding objects. To verify this suggestion, simulations of their evolution into the non linear regime have been performed. In fact, for selected models Glatzel, Kiriakidis, Chemigovski & Fricke (1999) found the velocity amplitude to exceed the escape velocity (see, however, Dor & Gautschi (2000)).

In this paper we report on a stellar model, which in the HRD is located well above the HD-limit, however, at lower effective temperature than the model studied by Glatzel, Kiriakidis, Chemigovski & Fricke (1999). As expected, this model turns out to be linearly unstable with dynamical growth rates. When following the non linear evolution of the instabilities, shocks form in the non linear regime. The latter is customary in pulsating stellar envelopes (see, e.g., Christy (1966)). Contrary to the "hotter" model studied by Glatzel, Kiriakidis, Chemigovski & Fricke (1999), however, these shocks are captured by the H-ionisation zone after a few pulsation periods. The captured shock starts to oscillate rapidly with periods of the order of the sound travel time across the H-ionisation zone, while its mean position changes on the dynamical timescale of the primary, strange mode instability. This phenomenon is described in detail in section 3.1. Assumptions and methods on which the calculations are based are given in section 2. We emphasise, that in this publication, we concentrate on the oscillations of the captured shock. The phenomenon of shock capture by H-ionisation itself is not investigated here and will be studied in a separate paper.

Apart from a detailed description of the shock oscillations found by numerical simulation the aim of the present paper consists of identifying their origin. This will be achieved by a linear stability analysis in section 3.2. It excludes a numerical

? E-mail: m.grott@uni-sw.gwdg.de (M G)

origin and attributes the oscillations to a secondary high frequency instability in the shock zone. To identify the physical origin of the instability an analytical model is constructed in section 4. Our conclusions follow.

2 BASIC ASSUMPTIONS AND METHODS

2.1 Construction of initial model

We investigate a stellar model having the mass $M = 50M_{\odot}$, chemical composition $X = 0.7$, $Y = 0.28$, $Z = 0.02$, effective temperature $T_e = 10^4 K$ and luminosity $L = 1.17 \times 10^6 L_{\odot}$. These parameters have been chosen to ensure instability of the model. In the Hertzsprung-Russell diagram (HRD) it lies within the instability region identified by Kiriakidis, Fricke & Glatzel (1993) (c.f. their figure 2). As only the envelope is affected by the instability, the model was constructed by standard envelope integration using the parameters given above. The stellar core and nuclear energy generation are disregarded. Convection is treated in the standard mixing-length theory approach with 1.5 pressure scale heights for the mixing length. The onset of convection was determined by the Schwarzschild criterion. For the opacities, the latest versions of the OPAL tables (Iglesias, Rogers & Wilson 1992; Rogers & Iglesias 1992) have been used.

2.2 Linear stability analysis

Having constructed a hydrostatic envelope model its stability with respect to infinitesimal, spherical perturbations is tested. The relevant equations corresponding to mass, energy and momentum conservation and the diffusion equation for energy transport are given in Baker & Kippenhahn (1962) (hereafter BKA):

$$\dot{\rho} = C_4 (3 + C_5 p - C_6 t) \quad (1)$$

$$\dot{l} = (i) C_1 (p + C_2 t) \quad (2)$$

$$\dot{p} = (4 + C_3 \rho^2) p \quad (3)$$

$$\dot{t} = C_7 (4 + C_{13} l + C_8 p - C_9 t) \quad (4)$$

ρ , l , p and t are the relative perturbations of radius, luminosity, pressure and temperature, respectively, and dashes denote derivatives with respect to $\ln p_0$. i is the eigenfrequency normalized to the inverse of the global free fall time $\tau_{ff} = \sqrt{R^3/3GM}$. The coefficients C_i are determined by the background model where C_{13} denotes the ratio of total and radiative luminosity. The other coefficients are defined in BKA. For the general theory of linear non-adiabatic stability, we refer the reader to Cox (1980) and Unno et al. (1989).

The coupling between pulsation and convection is treated in the standard frozen in approximation, i.e., the Lagrangian perturbation of the convective flux is assumed to vanish. This is justified since the convective flux never exceeds 10% of the total energy flux. Moreover, the convective time scale is much longer than the dynamical time scale of the pulsations considered. The solution of the perturbation problem has been determined using the Riccati method (Gautschi & Glatzel 1990). As a result of the linear non-adiabatic (LNA) stability analysis we obtain periods and growth or damping rates of various modes together with the associated eigenfunctions.

2.3 Non-linear evolution

Having identified an instability by the LNA analysis its growth is followed into the non-linear regime. Assuming spherical symmetry, we adopt a Lagrangian description and choose as independent variables the time t and the mass m inside a sphere of radius r . The evolution of an instability is then governed by mass conservation,

$$\frac{\partial r^3}{\partial m} - \frac{3}{4} = 0 \quad (5)$$

momentum conservation,

$$\frac{\partial^2 r}{\partial t^2} + 4 r^2 \frac{\partial p}{\partial m} + \frac{Gm}{r^2} = 0 \quad (6)$$

energy conservation,

$$\frac{\partial L}{\partial m} - \frac{p}{r^2} \frac{\partial}{\partial t} + \frac{\partial E}{\partial t} = 0 \quad (7)$$

and the diffusion equation for energy transport,

$$\frac{\partial T}{\partial m} - \frac{3}{64} \frac{(L - L_{\text{conv}})}{a c r^4 T^3} = 0 \quad (8)$$

Table 1. Unstable modes of the initial model.

τ	0.53	1.22	1.66	2.12	2.26	3.34	3.86
i	-0.06	-0.18	-0.13	-0.20	-0.12	-0.04	-0.04

τ denotes the real part and i the imaginary part of the eigenfrequency normalized by the global free fall time.

where ρ , p , T , L , and E denote density, pressure, temperature, luminosity and specific internal energy, respectively. a is the radiation constant, c the speed of light and G the gravitational constant. For consistency, the equation of state $p(\rho; T)$ and the opacity κ are identical with those used for the construction of the initial model. In accordance with the LNA stability analysis, convection is treated in the frozen in approximation, i.e., L_{conv} is taken to be constant during the non-linear evolution and equal to the initial value. For the treatment of shocks artificial viscosity is introduced by substituting $P = P + Q$ with (v is the velocity)

$$Q = \begin{cases} C_0 (\text{div } v)^2 & \text{div } v < 0 \\ 0 & \text{div } v > 0 \end{cases} \quad (9)$$

and $C_0 > 0$ (von Neumann-Richtmyer form of artificial viscosity).

For some difference schemes including the Fraley scheme, which the present method is based on, this form of the artificial viscosity can give rise to undesired, unphysical oscillations (see, e.g., Buchler & Wahlen (1990)). To avoid these, artificial tensor viscosity is usually used (Tschamuter & Winkler (1979)). In order to be sure that the oscillations observed are not caused by the form of the artificial viscosity, we have run tests both with volume and tensor viscosity. As a result, shock oscillations are found independently for any form of the artificial viscosity. As the von Neumann-Richtmyer viscosity allows for a straightforward formulation of the boundary conditions discussed below, we have for convenience chosen to work with it.

The inert hydrostatic core provides boundary conditions at the bottom of the envelope by prescribing its time independent radius and luminosity there. As the outer boundary of the model does not correspond to the physical boundary of the star, boundary conditions are ambiguous there. We require the gradient of heat sources to vanish there:

$$\text{grad}(\text{div } F) = 0 \quad (10)$$

This boundary condition is chosen to ensure that outgoing shocks pass through the boundary without reflection. The numerical code relies on a Lagrangian, with respect to time implicit, fully conservative difference scheme proposed by Fraley (1968) and Samarskii & Popov (1969). Concerning tests of the code, we adopted the same criteria as Glatzel, Kiriakidis, Chemigovskij & Fricke (1999).

3 NUMERICAL RESULTS

3.1 The evolution of the stellar model

Density and temperature of the initial model as a function of relative radius, are shown in figures 1a1-1a2. The stratification exhibits a pronounced core-envelope structure, which is typical for stellar models in this domain of the HRD. More than 96 per cent of the mass is concentrated in the core, which extends to less than 5 per cent of the total radius. It remains in hydrostatic equilibrium and is not affected by the instability.

The initial model has been tested for stability and been found unstable on dynamical timescales. This instability will be referred to as primary instability hereafter. With respect to its physical origin, it is a strange mode instability, which has been identified in a variety of stars including Wolf-Rayet stars, H dC stars and massive stars (like the present model). Strange modes appear as mode coupling phenomena with associated instabilities whenever radiation pressure is dominant. The latter is true for a large fraction of the radius in the present model. The linear stability analysis of the initial model reveals several unstable modes. Eigenfrequencies of the most unstable ones, i.e., their real (τ) and imaginary parts (i), are presented in table 1.

The evolution of the linear instabilities was followed into the non-linear regime by numerical simulation using the hydrostatic model as initial condition. No additional initial perturbation of the hydrostatic model was added. Rather the code was required to pick the correct unstable modes from numerical noise. By comparing growth rates and periods obtained in the simulation with the results of the LNA analysis, the linear regime of the evolution was used as a test for the quality of the simulation.

In the non-linear regime sound waves travelling outwards form shocks and initially inflate the envelope to 2.5 initial radii. Thus velocity amplitudes of 10^7 [cm/sec] are reached. One of the subsequent shocks is captured around the H-ionization zone at relative radius $r/R = 0.58$ and $3.6 < \log T < 4.7$. The mechanism responsible for the shock capturing will not be studied

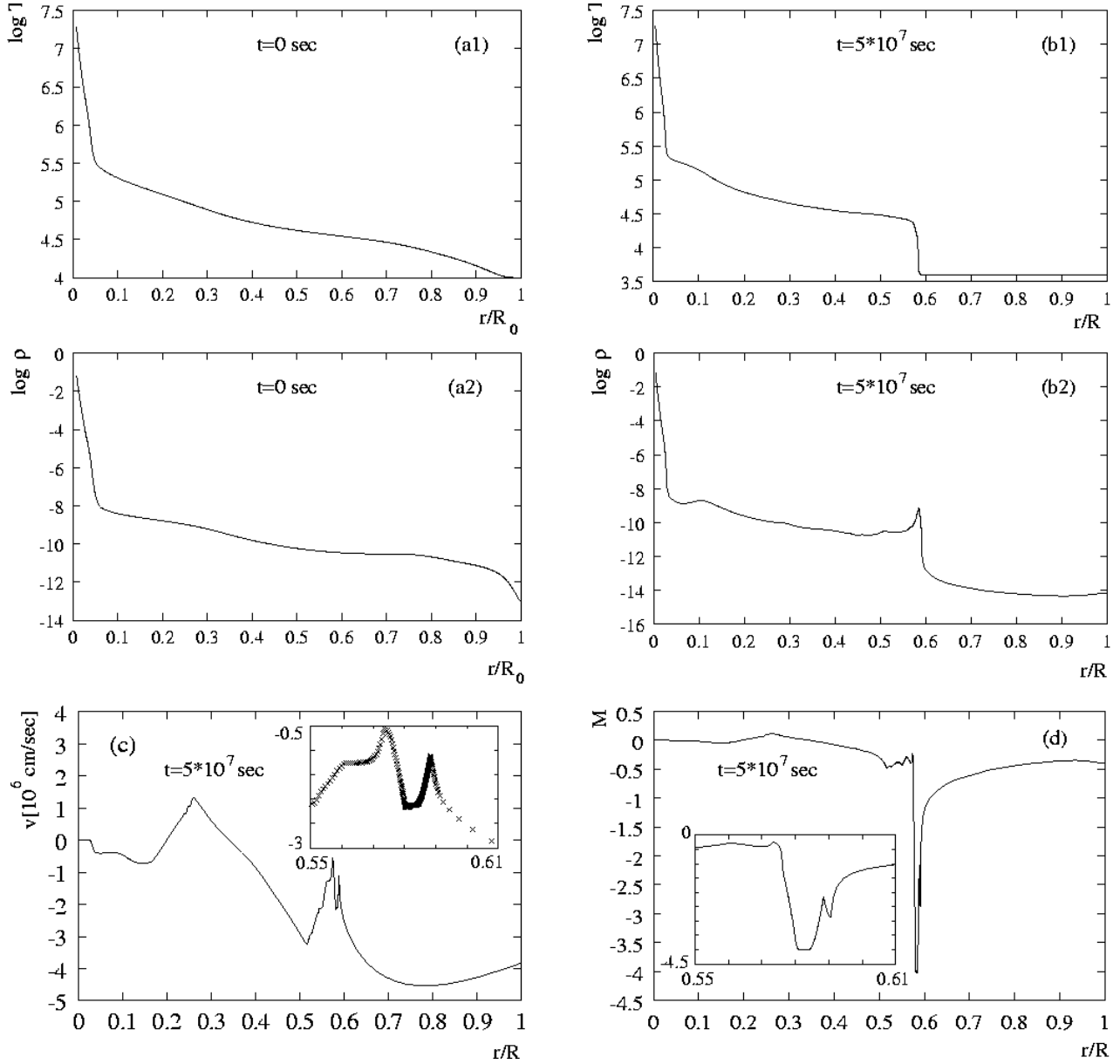


Figure 1. Temperature T and density ρ as a function of relative radius of the initial model (a1-a2), and the model at 5×10^7 sec (b1-b2). Velocity v and Mach number M are shown as a function of relative radius for the model at 5×10^7 sec in (c) and (d), respectively.

in this publication. Rather, we will investigate the oscillations on the shock front and show that they are of physical origin. A snapshot at time $t = 5 \times 10^7$ sec of the situation containing the captured shock is shown in Figures 1b1 and 1b2. Figure 1c shows the velocity as a function of relative radius at this instant. Sound waves are generated in the region around $r/R \approx 0.1$ and travel outwards, growing in amplitude and steepening. In the snapshot one such wave is located at $r/R \approx 0.25$. The captured shock front is located at $r/R \approx 0.58$ and the outer envelope is collapsing onto it. The small panel in Figure 1c shows the details of the region containing the captured shock, indicating the grid resolution by (x). Within the Lagrangian description, 150 of the 512 gridpoints used are concentrated in the shock zone. Figure 1d shows the Mach number $M = v/v_s$ as a function of relative radius for the snapshot (v_s is the local sound speed). The Mach number changes by 3.5 across the shock front around $r/R \approx 0.58$.

After the formation of the captured shock its position varies only weakly by ≈ 0.2 relative radii on the timescale of the primary instability (see Figure 2b). Superimposed on this variation is a much faster oscillation, whose timescale is related to the sound travel time across the shock ($\approx 10^6$ sec). It is even more pronounced in the run of the luminosity (Figure 2c2). The onset of the fast oscillation with the capturing of the shock by the H-ionization-zone is illustrated in Figures 2a and 2c1, where the velocity v and relative luminosity L/L_0 at the outer boundary are shown as a function of time. Up to 4×10^6 sec the velocity varies on the timescale of the primary instability and the luminosity remains approximately constant due to the

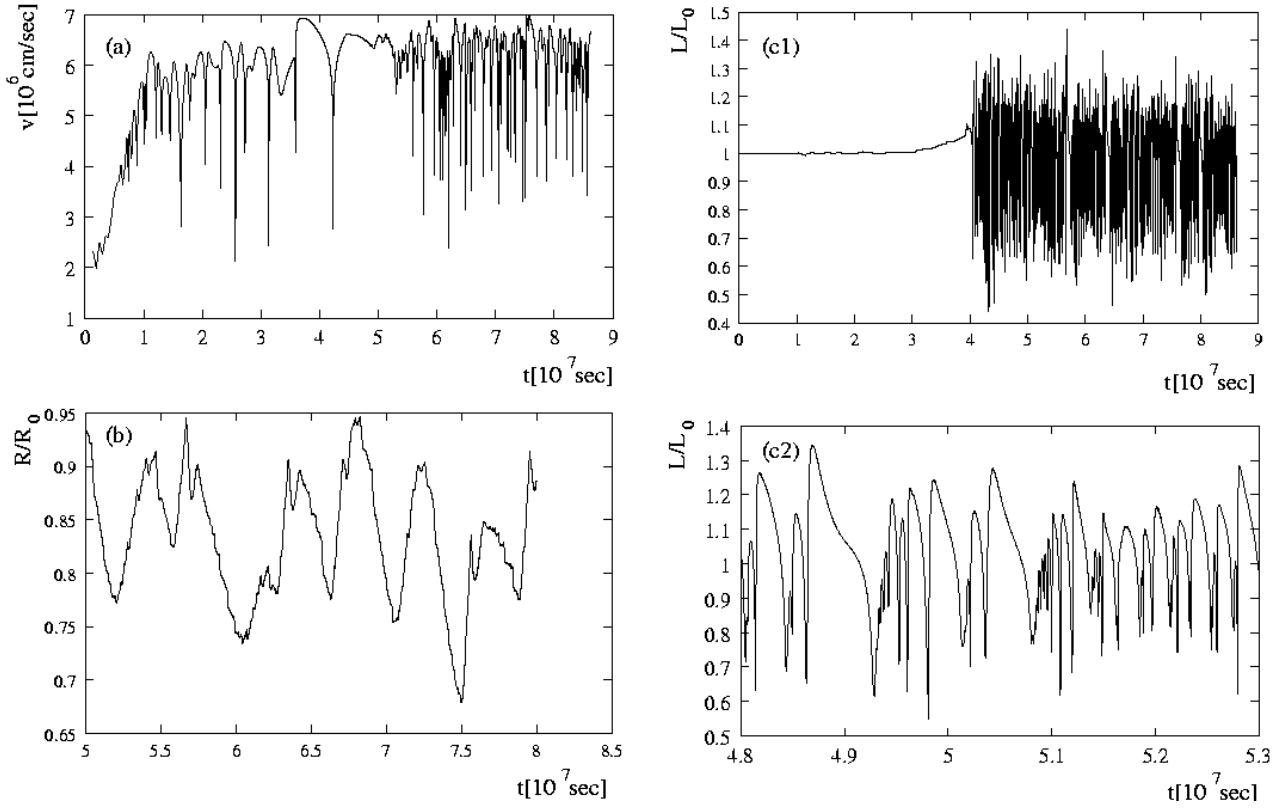


Figure 2. The velocity v at the boundary (a), the relative position of the shock front (b) and the relative luminosity $L=L_0$ at the boundary on two different scales (c1-c2) as a function of time t .

low heat capacity of the envelope of the star. After $t = 4 \cdot 10^7$ sec, when the shock has been captured by the H-ionization-zone, luminosity and velocity vary on the shorter time scale of the secondary shock oscillation. The luminosity perturbation has its origin in the shock. Due to the low heat capacity the luminosity perturbation remains spatially constant above the shock.

In principle, the high-frequency secondary oscillations of the shock could be caused numerically. However, the results are largely independent of the numerical treatment and parameters, which has been verified by extensive numerical experiments suggesting a physical origin of the phenomenon. In section 3.2, we shall argue in favour of the latter by presenting a linear stability analysis providing an instability with appropriate frequencies and growth rates.

3.2 Stability analysis of a model containing a captured shock

In this Section we shall initially assume and then prove a posteriori, that the secondary oscillations of the captured shock described in section 3.1 are caused by physical processes. We perform a linear stability analysis of a background model by assuming that the dependent variables radius, pressure, temperature and luminosity may be expressed as the sum of a background contribution and a small perturbation:

$$x(m; t) = x_0(m; t) + x_1(m; t) \quad \text{for } x \in \{r, p, T, L, g\} \quad (11)$$

The background coefficients $x_0(m; t)$ may be regarded as time independent, i.e., $x_0(m; t) = x_0(m)$, as long as the perturbations vary on much shorter time scales as the background, i.e., as long as the condition

$$\frac{d \log x_0(m; t)}{dt} \ll \frac{d \log x_1(m; t)}{dt} \quad (12)$$

holds. $\frac{d}{dt}$ denotes the Lagrangian time derivative. Thus, the variations on dynamical time scales of the model containing the captured shock are regarded as stationary with respect to the anticipated much faster instability. Eigenmodes with periods of the order of the dynamical time scale suffer from the competition with the variation of the "background" model, whereas the approximation holds for those with much shorter periods. For the model considered, the approximation is correct for $j > 100$. Should unstable eigenmodes of this kind exist, this would prove the instability and the high frequency oscillations of the captured shocks to be of physical origin. Therefore, the results of a linear stability analysis of such a model are meaningful, as long as the obtained frequencies are interpreted properly.

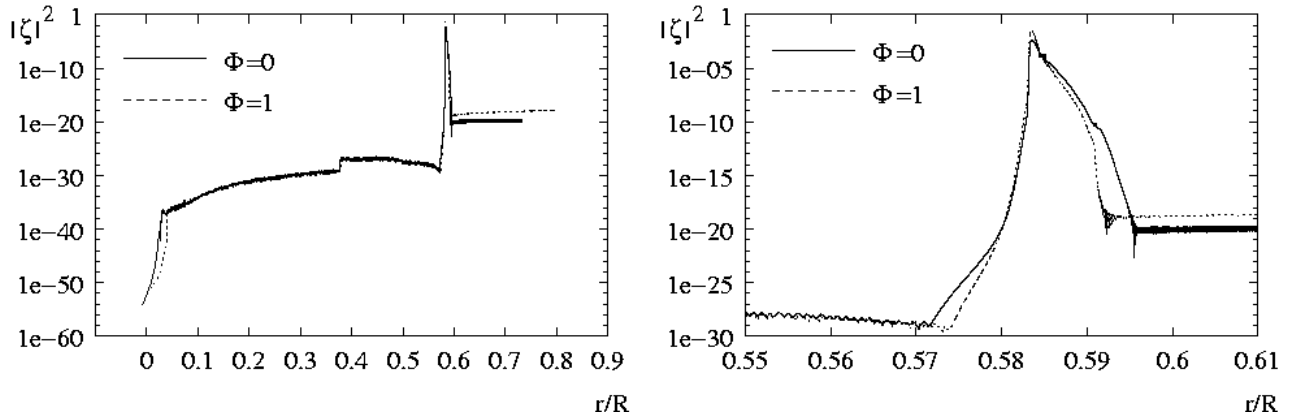


Figure 3. Modulus of the Lagrangian displacement as a function of relative radius for the eigenfrequencies $\omega_r = 4651.7$, $\omega_i = 119.6$ ($\Phi = 0$, solid lines) and $\omega_r = 4837.2$, $\omega_i = 83.9$ ($\Phi = 1$, dotted lines). The right panel shows details for the shock zone.

A problem with this strategy is that the numerical simulations provide only the superposition of the slow dynamical and the secondary, fast oscillations. The linear stability analysis, however, requires a – on the fast oscillations – stationary background model. It is obtained by an appropriate time average over a numerically determined sequence of models. “Appropriate” means, that the average has to be taken over times longer than the short period oscillations and shorter than the dynamical timescale. Thus all physical quantities $Q(m; t)$ are averaged according to

$$\langle Q(m) \rangle = \frac{1}{t_e - t_b} \int_{t_b}^{t_e} Q(m; t) dt \quad (13)$$

where t_b and t_e are the beginning and the end of the averaging interval and satisfy the requirements discussed above. t_b has been varied between 4 $\times 10^5$ sec and 5 $\times 10^5$ sec (after the formation of the shock front) and the averaging interval between 5 $\times 10^5$ sec and 1 $\times 10^6$ sec. All averages exhibit qualitatively the same behaviour and the LNA stability analysis is largely independent of the averaging parameters. The results presented in the following were obtained for $t_b = 5 \times 10^5$ sec and $t_e = 5.05 \times 10^5$ sec.

With these assumptions, the linear perturbation equations 1-4, which have been derived for a strictly static background model, remain valid even for the situation studied here, except for the momentum equation 3, which has to be modified according to:

$$p^0 = (4 + C_3^{-2}) Q_1 p \quad \text{with} \quad Q_1 = \frac{\partial p_0 / \partial m}{\partial p_0 / \partial m} \quad (14)$$

$Q_1 \neq 1$ accounts for the deviations from hydrostatic equilibrium.

As a result of the linear stability analysis (with $Q_1 \neq 1$), the expected unstable modes having high frequencies have been identified. E.g., a typical mode of this kind satisfying the assumptions discussed has the frequency $\omega_r = 4837.2$ and the growth rate $\omega_i = 83.9$.

In a second step, we investigate the influence of deviations from hydrostatic equilibrium, i.e., the deviations from $Q_1 = 1$. For this purpose we rewrite equation 14 as

$$p^0 = (4 + C_3^{-2}) p + (1 - Q_1) p \quad (15)$$

with $0 \leq Q_1 \leq 1$. The limits $Q_1 = 0$ and $Q_1 = 1$ correspond to hydrostatic equilibrium and the averaged model containing the shock, respectively. The influence of deviations from hydrostatic equilibrium is then studied by varying Q_1 between 0 and 1. Following the mode having $\omega_r = 4837.2$ and $\omega_i = 83.9$ at $Q_1 = 1$ to $Q_1 = 0$ its frequency and growth rate changes to $\omega_r = 4651.7$ and $\omega_i = 119.6$. The moduli of the corresponding Lagrangian displacements, which indicate the kinetic energy of the pulsations, are shown in Figure 3 as a function of relative radius. The energy of the pulsation is concentrated around $r/R \approx 0.58$ and drops off exponentially above and below. As a result, neither eigenvalues nor eigenfunctions differ significantly for $Q_1 = 0$ and $Q_1 = 1$, i.e., the assumption of hydrostatic equilibrium is justified for the unstable modes considered. Therefore, we will assume hydrostatic equilibrium in a further discussion and investigation of the secondary instability, i.e., all subsequent results were obtained assuming $Q_1 = 0$.

The results of a LNA stability analysis according to equations 1-4 and Section 2.2 for the averaged model are summarized in Table 2, where representative values for the eigenfrequencies of unstable modes are given. Three sets of unstable modes may be distinguished. Low order modes with ω_r between 0.9 and 9 have growth rates of the order of 0.2, i.e. a ratio of $\frac{\omega_i}{\omega_r} \approx 0.1$. They can be identified with the primary instability. However, their periods compete with the variation of the background model and therefore these modes have to be interpreted with caution. The properties of two classes of high order unstable modes with frequencies ω_r between 140 and 4650 are in accordance with our approximation. One of them has high growth

Table 2. Unstable modes of the averaged model

ω_r	0.92	2.22	3.31	4.74	6.08	7.48	8.79	10.1	11.4	140.4
ω_i	-0.05	-0.33	-0.32	-0.25	-0.29	-0.18	-0.21	-0.24	-0.12	-0.1
ω_r	154.4	162.9	157.2	179.6	202.0	413.6	447.3	487.5	541.4	4651.7
ω_i	-0.05	-35.4	-0.08	-27.8	-17.6	-30.4	-26.3	-54.9	-0.35	-119.6

ω_r denotes the real part and ω_i the imaginary part of the eigenfrequency normalized by the global free fall time.

rates with a ratio of $\frac{\omega_i}{\omega_r} \approx 0.1$, the second low growth rates with a ratio of $\frac{\omega_i}{\omega_r} \approx 5 \cdot 10^{-4}$. The latter may be identified with high order primary instabilities, whereas the former are attractive candidates for the secondary, shock front instabilities sought.

For further discussion, we consider eigenfunctions and the corresponding work integrals of representative members of the different sets of modes. The work integral is a widely used tool to identify the regions in a star, which drive or damp the pulsation. Glatzel (1994) has shown, that the concept of the work integral is not necessarily restricted to small values of the damping or growth rate. By replacing the conventional time average by an ensemble average it can be extended to arbitrary values of $\frac{\omega_i}{\omega_r}$. In any case, one arrives at the expression

$$W(r) = \frac{i}{\omega_r} \int_0^{\omega_r} r^2 \bar{p} \operatorname{Im} (p^y)^y dr^0 \quad (16)$$

for the work integral, where $\operatorname{Im}(z)$ denotes the imaginary part of z , $()^y$ denotes complex conjugation and $p^y, {}^y p$ denote the spatial parts of the eigenfunctions of the relative pressure and density perturbations, respectively. \bar{p} is the pressure of the background model. The sign of the integrand in equation 16 determines, if a region of the star damps or drives the pulsation, where $\operatorname{Im} (p^y)^y < 0$ corresponds to driving and $\operatorname{Im} (p^y)^y > 0$ to damping. Some authors (e.g. BKA) use $\log p$ instead of r as independent variable and therefore obtain an opposite sign of the differential work integral for driving and damping in unence. To match this convention, $W(r)$ is shown in figures 4b, i.e., driving regions correspond to positive $W(r)$, damping regions to negative $W(r)$.

According to its eigenvalues the mode corresponding to $\omega_r = 2.22$, $\omega_i = -0.33$ was identified as a primary instability. This is supported by the Lagrangian displacement component of the eigenfunction and the work integral shown in figure 4a1 and 4b1. The shock front acts as an acoustic barrier causing the eigenfunction to vanish above it (figure 4a1). The work integral (figure 4b1) exhibits two driving regions which coincide with the opacity peaks at $\log T = 5.3$ (caused by the contributions of heavy elements) and $\log T = 4.7$ (He-ionization). The stability properties are not affected significantly by the shock region.

The counterparts of figures 4a1 and 4b1 for a weakly unstable high frequency mode having $\omega_r = 157.2$, $\omega_i = -0.08$ are shown in figures 4a2 and 4b2. Again, the isolating effect of the shock front causes the dramatic variation of the amplitude around $r=R_0 = 0.6$. However, in contrast to the eigenfunction presented in figure 4a1 the amplitude is now significant above and negligible below the shock. High order modes of this kind in general exhibit strong damping. For the mode considered the shock efficiently screens the inner damping part of the stellar envelope. Thus the region below the shock contributes only weak damping which is overcome by the driving in unence of the shock as shown by the work integral in figure 4b2.

Apart from splitting the acoustic spectrum by an acoustic barrier into two sets of modes associated with the acoustic cavities below and above the shock, respectively, the shock itself gives rise to a third set. Lagrangian displacement and work integral for a typical member of this set having $\omega_r = 162.9$, $\omega_i = -35.4$ are shown in figures 4a3 and 4b3. The amplitude of this unstable mode reaches its maximum on the shock and drops off exponentially above and below. Note its oscillatory behaviour on and close con nement to the shock. The real parts of this set of eigenfrequencies of ≈ 200 – 500 correspond to periods of $\approx 8 \cdot 10^{-2}$ – 10^{-3} sec, which are observed in the luminosity perturbations (cf. figure 2c2) induced by the shock oscillations. The work integral (figure 4b3) shows, that the shock is driving this instability, and that the regions above and below do not contribute. Moreover, the basic assumption of stationarity of the averaged model holds for the frequencies and growth rates obtained.

Thus we have identified an instability by linear analysis of an averaged model, which resembles the shock oscillations observed in the numerical simulations, both with respect to timescales and spatial structure. We therefore conclude, that the shock oscillations are not numerical artifacts. Rather they have a physical origin and are caused by an instability whose mechanism will be investigated in detail in the following sections.

3.3 Approximations

In order to gain further insight into the physical processes responsible for the instability, different approximations in equations (1)–(4) have been considered. To obtain a continuous transition from the exact treatment to the approximation, we introduce

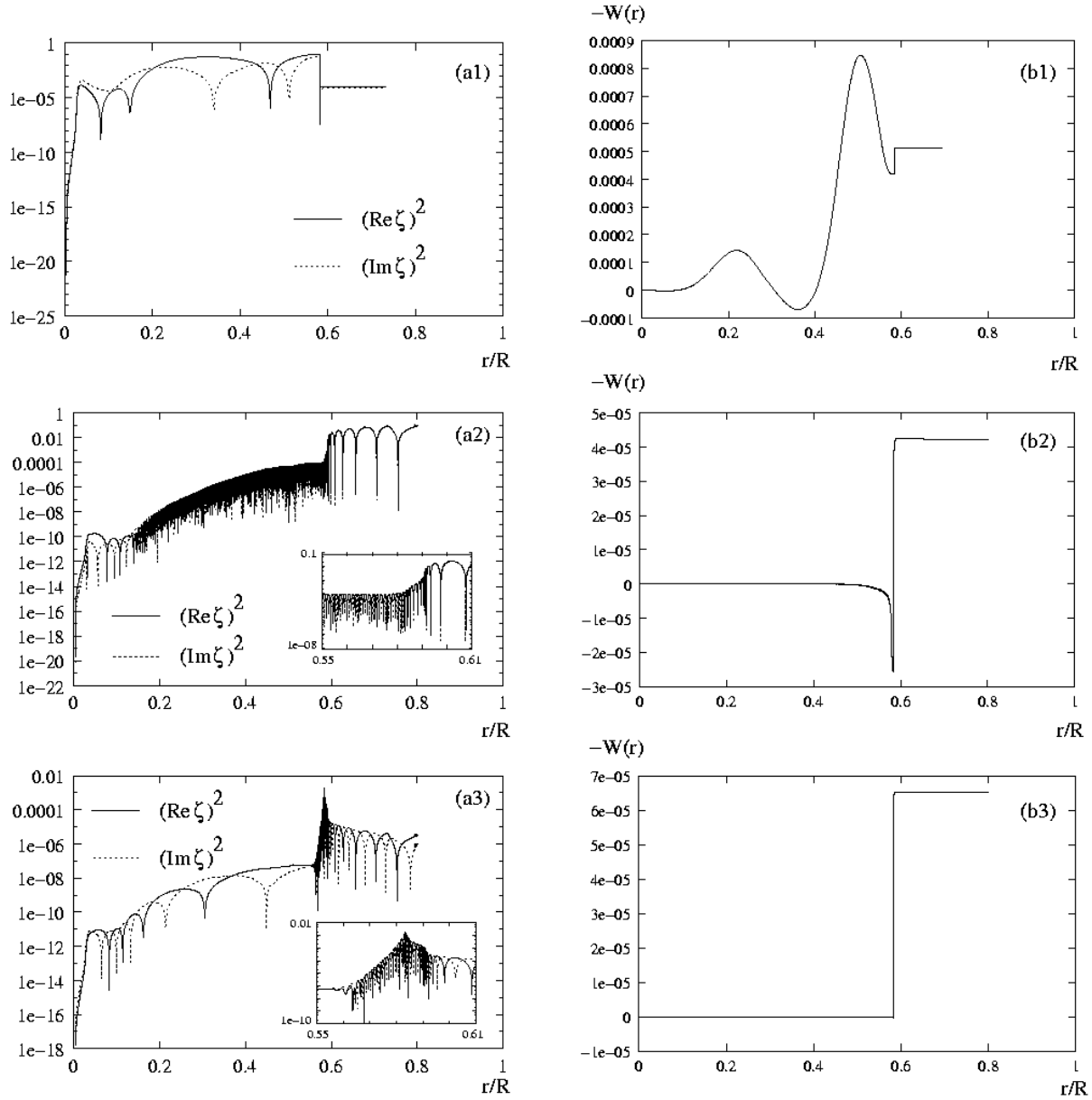


Figure 4. Lagrangian displacements (a) and integrated workintegrals (b) as a function of relative radius for the eigenfrequencies $r_s = 2.22$, $i_s = 0.33$ (1), $r_s = 157.2$, $i_s = 0.08$ (2) and $r_s = 162.9$, $i_s = 35.4$ (3) of the averaged model.

a parameter α with $\alpha = 1$ corresponding to the exact problem and $\alpha \rightarrow 0$ to the approximation. The numerical results, i.e. the eigenvalues of the shock front instabilities, are followed as a function of α .

Introducing α into the Euler equation as

$$p^0 = (4 + \alpha^2) p \quad (17)$$

the limit $\alpha \rightarrow 0$ corresponds to vanishing acceleration and implies the elimination of acoustic modes from the spectrum, which then only consists of secular modes. Application of this limit to the shock instabilities has not revealed any unstable modes. Rather the eigenvalues have diverged. This excludes a thermal origin of both the unstable modes and the instability mechanism. For a proper treatment of the instability, the mechanical acceleration has to be taken into account.

Introducing α into the equation for energy conservation as

$$\dot{I}^0 = C_1 (i) (p + C_2 t) \quad (18)$$

the adiabatic limit is obtained by $\alpha \rightarrow 1$. The latter implies $(p + C_2 t) = 0$, i.e. the algebraic adiabatic relation between

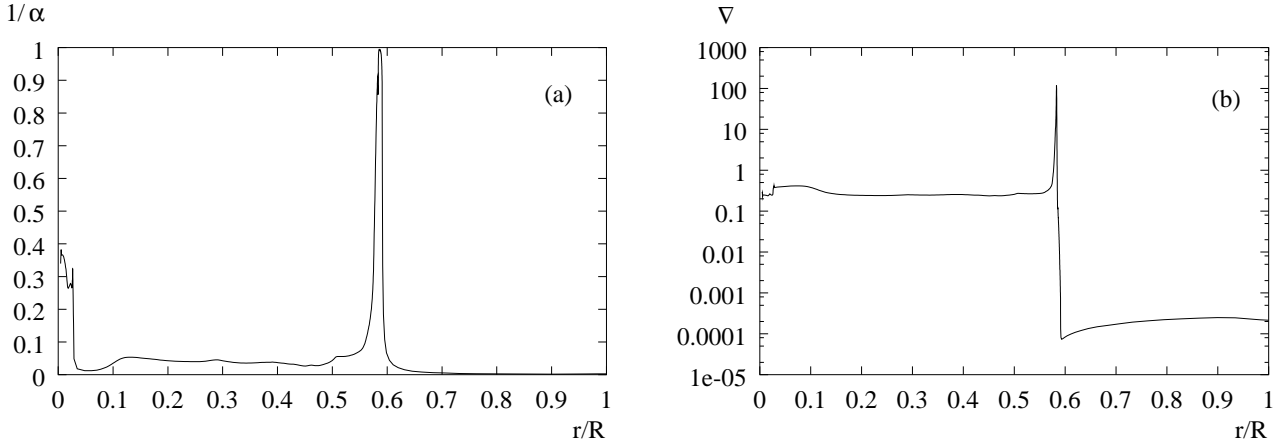


Figure 5. The coefficients $C_5 = 1/\alpha$ (a) and $C_7 = \gamma$ (b) of the averaged model as a function of relative radius.

pressure and temperature perturbation. No unstable modes have been found following the shock instabilities into the adiabatic limit.

Introducing into the equation for energy conservation as

$$\dot{T}^0 = C_1 \quad (i) \quad (p + C_2 t) \quad (19)$$

$\dot{T}^0 = 0$ corresponds to the so called NAR-limit (Non-Adiabatic-Reversible limit) (Gautschi & Glatzel 1990). Although this approximation – like the adiabatic approximation – implies constant entropy, it does not represent the adiabatic limit ($p + C_2 t = 0$). Rather it is equivalent to $C_1 = 0$. Since C_1 is related to the thermal and dynamical timescales τ_{th} and τ_{dyn} by

$$C_1 = \frac{\tau_{th}}{\tau_{dyn}} r_{ad} \frac{C_3 C_4}{C_3 C_4} \quad (20)$$

this approximation is also being referred to as the zero thermal timescale approximation (τ_{th} and r_{ad} are the adiabatic indices). Physically, it means that the specific heat of the envelope is negligible and luminosity perturbations cannot be sustained. In particular, this approximation rules out the classical mechanism as the source of an instability – should it exist in the NAR-limit – since this Carnot-type process relies on a finite heat capacity. When following the frequencies of the modes belonging to the shock front instabilities into the NAR-limit, periods and growth rates change only slightly (by at most 10 per cent). Thus the NAR-approximation may be regarded as a satisfactory approximation and will form the basis of our investigations in the following sections.

4 ANALYTICAL MODEL

4.1 Three-Zone-Model

The modal structure identified in section 3.2 with three sets of modes associated with three acoustic cavities (inner envelope, shock and outer envelope) suggests the construction of a three zone model. In order to enable an analytical solution, the coefficients of the differential equations are kept constant in each zone.

According to the previous section the NAR-approximation is sufficient to describe the shock front instabilities. The equation of energy conservation is then satisfied identically and luminosity perturbations vanish. Thus we are left with a system of third order comprising the mechanical equations and the diffusion equation with zero luminosity perturbation.

Further reduction of the order of the differential system is achieved by considering its coefficients which depend on the properties of the averaged model. In figure 5 the coefficients $C_5 = \frac{\partial \log \gamma}{\partial \log p} = \frac{1}{\gamma}$ and $C_7 = \gamma = \frac{d \log T}{d \log p}$ are shown as a function of relative radius. γ denotes the ratio of gas pressure to total pressure. The coefficients $C_4 = \frac{d \log r}{d \log p}$ and $C_3 = \frac{4}{3} \frac{r^3}{M_r}$ may be regarded as constant all over the envelope. Approximate values are $C_4 = \frac{1}{3}$ and $C_3 = 3$. The latter holds because almost the entire mass is concentrated in the stellar core. From figure 5 we deduce that radiation pressure is dominant except for the shock zone. Therefore we replace the diffusion equation 4 by the algebraic equation of state for pure radiation ($p = 4t$) in the inner and outer envelope. On the other hand $C_7 = \gamma$ can – to first approximation – be regarded as singular in the shock zone. According to equation 4 this requires the expression $(4 + C_8 p - C_9 t)$ to vanish there. Thus the differential diffusion equation is replaced by an algebraic relation in all three zones, reducing the system to second order.

Adopting the alternative notation (Baker & Kippenhahn 1962) $C_6 = \beta$, $C_8 = \beta$ and $C_9 = 4 - \beta$, where β is the negative

logarithmic derivative of density with respect to temperature at constant pressure, ρ_p the logarithmic derivative of opacity with respect to pressure at constant temperature and ρ_T the logarithmic derivative of opacity with respect to temperature at constant pressure, and choosing the relative radius x as the independent variable, we are left with the following set of equations:

$$\frac{1}{x} \frac{d}{dx} = \frac{1}{3} (3 + \rho_p - \rho_T) \quad (21)$$

$$\frac{1}{x} \frac{dp}{dx} = \frac{1}{4} (4 + 3\rho_p^2) - \rho_p \quad (22)$$

$$\rho_T = \begin{cases} < \frac{1}{4} \frac{1}{\rho_p} (\rho_p^2 - 4) & x \in [a; b] \\ \frac{1}{4} \rho_p & x \in [0; a) \text{ or } x \in (b; 1] \end{cases} \quad (23)$$

a and b denote the lower and upper boundary of the shock zone. The transformation of the independent variables $\ln p_0 \rightarrow x$ introduces the factor $\frac{1}{C_4 x}$, which is constant within the framework of the three-zone model, and given by an appropriate mean of the quantity $\frac{1}{C_4 x}$. In general ρ_T is negative and of order unity.

We are thus left with a system of second order consisting of the mechanical equations (continuity and Euler equations) which is closed by the algebraic relations $0 = 4 + C_8 p - C_9 \rho_T$ and $p = 4 - \rho_T$ for the shock region and the inner/outer regions, respectively. We rewrite it as:

$$\frac{d}{dx} = A_{1;2} + B_{2;2} p \quad (24)$$

$$\frac{dp}{dx} = C + D p \quad (25)$$

where

$$A_{1;2} = \begin{cases} < 1 + \frac{4}{3} \frac{1}{\rho_T} & x \in [a; b] \\ \frac{1}{3} & x \in [0; a) \text{ or } x \in (b; 1] \end{cases} \quad (26)$$

$$B_{1;2} = \begin{cases} < \frac{1}{3} \frac{\rho_p}{4 - \rho_p} & x \in [a; b] \\ \frac{1}{3} & x \in [0; a) \text{ or } x \in (b; 1] \end{cases} \quad (27)$$

$$C = \begin{cases} < \frac{1}{3} \frac{\rho_p}{4 - \rho_p} & x \in [a; b] \\ \frac{1}{3} & x \in [0; a) \text{ or } x \in (b; 1] \end{cases} \quad (28)$$

$$D = \begin{cases} < \frac{1}{3} \frac{\rho_p}{4 - \rho_p} & x \in [a; b] \\ \frac{1}{3} & x \in [0; a) \text{ or } x \in (b; 1] \end{cases} \quad (29)$$

$$C = \frac{1}{3} (4 + 3\rho_p^2) \quad (30)$$

$$D = \frac{1}{3} \rho_p \quad (31)$$

and the subscript 1 denotes the values of the coefficients in the shock region, the subscript 2 values in the inner and outer regions. We introduce new variables by

$$\hat{p} = e^{\int A_{1;2} dx} \quad (32)$$

$$\hat{p} = e^{\int D dx} p \quad (33)$$

The system 24-25 then reads

$$\frac{d\hat{p}}{dx} = B_{1;2} \hat{p} e^{\int D dx} e^{\int A_{1;2} dx} \quad (34)$$

$$\frac{d\hat{p}}{dx} = C \hat{p} e^{\int D dx} e^{\int A_{1;2} dx} \quad (35)$$

These equations are equivalent to the following single second order equation:

$$\frac{d}{dx} \left(\frac{1}{C} e^{\int D dx} e^{\int A_{1;2} dx} \frac{d\hat{p}}{dx} \right) - e^{\int D dx} e^{\int A_{1;2} dx} B_{2;2} \hat{p} = 0 \quad (36)$$

4.1.1 Mathematical Structure of the Problem

Equation 36 may be written as

$$\frac{d}{dx} \left(e^{\int D dx} e^{\int A_{1;2} dx} \frac{d\hat{p}}{dx} \right) + 4 e^{\int D dx} e^{\int A_{1;2} dx} B_{2;2} \hat{p} + 3 e^{\int D dx} e^{\int A_{1;2} dx} B_{2;2} \hat{p} = 0 \quad (37)$$

and has the form

$$\frac{d}{dx} \left(q(x) \frac{d\hat{p}}{dx} \right) + w(x) \hat{p} + u(x) \hat{p} = 0 \quad (38)$$

with $q(x) > 0$ in the integration interval. However, $u(x)$ is positive in the inner and outer regions and negative in the shock region, i.e., $u(x)$ changes sign in the integration interval. (This holds also for $w(x)$.) Therefore, this problem is not of Sturm-Liouville type. On the other hand, if we consider each zone separately with boundary conditions $\dot{p} = 0$, equation 38 describes a Sturm-Liouville problem. In the shock zone we define eigenvalues $\omega_j^2 = \omega_j^2$ and thus have $u(x) > 0, w(x) > 0$, for the inner and outer zones we get $u(x) > 0, w(x) < 0$ by defining $\omega_j^2 = -\omega_j^2$.

For a Sturm-Liouville problem, the eigenvalues are real and form a sequence

$$\omega_1^2 < \omega_2^2 < \omega_3^2 < \omega_4^2 < \dots \quad (39)$$

Furthermore, ω_1 may be estimated on the basis of the variational principle

$$\omega_1 = \min_p \frac{\int_0^{R_1} q(x) \dot{p}^2 dx + \int_0^{R_1} w(x) \dot{p}^2 dx}{\int_0^{R_1} u(x) \dot{p}^2 dx} \quad (40)$$

Therefore $\omega_1^2 = \omega_1^2$ is positive in the shock zone, since $w(x)$ is positive there. This means that we have purely imaginary eigenfrequencies $\omega_j = i \omega_j$ with positive ω_j and

$$\omega_1 < \omega_2 < \omega_3 < \omega_4 < \dots \quad (41)$$

Thus the shock zone provides unstable eigenfrequencies.

Since $w(x)$ is negative in the inner and outer zones, we cannot guarantee ω_1 to be positive there. For sufficiently large j , however, ω_j will always become positive. As a consequence, all eigenfrequencies $\omega_j = i \omega_j$ will become real for sufficiently high order $j > n$ and satisfy:

$$\omega_n < \omega_{n+1} < \omega_{n+2} < \omega_{n+3} < \dots \quad (42)$$

In principle, the mathematical structure of the problem allows for imaginary pairs of eigenfrequencies at low orders in the inner and outer zones. For the particular parameters studied in the following sections, however, ω_1 turned out to be positive, i.e., $n = 1$ and all eigenfrequencies are real.

Even if equation 37 together with the boundary conditions $\dot{p} = 0$ at $x = 0$ and $x = 1$ (three-zone model) is not of Sturm-Liouville type, the differential operator

$$D = \frac{d}{dx} q \frac{d}{dx} + u - w \quad (43)$$

in equation 38 can be shown to be self adjoint with the boundary conditions $\dot{p} = 0$ at $x = 0$ and $x = 1$. Therefore the eigenvalues are real and we do expect only real or purely imaginary eigenfrequencies, i.e., we will not be able to reproduce the complex eigenfrequencies of the exact problem in this approximation.

4.1.2 Results

Assuming the coefficients C and $B_{1,2}$ to be constant, equations 34 and 35 are solved by the Ansatz $\dot{p};^{\wedge} / e^{kx}$. For the wavenumbers k we get

$$k = \frac{p}{B_{1,2} C} \quad (44)$$

Thus the general solutions reads

$$\dot{p} = \begin{matrix} \sum_{a=1}^8 \\ \sum_{b=1}^2 \\ \sum_{c=1}^2 \end{matrix} \begin{matrix} a_1 e^{\frac{p}{B_2 C} x} + a_2 e^{\frac{p}{B_2 C} x} \\ b_1 e^{\frac{p}{B_1 C} x} + b_2 e^{\frac{p}{B_1 C} x} \\ c_1 e^{\frac{p}{B_2 C} x} + c_2 e^{\frac{p}{B_2 C} x} \end{matrix} \quad \begin{matrix} x \in [0; a) \\ x \in [a; b] \\ x \in (b; 1] \end{matrix} \quad (45)$$

$a_{1,2}, b_{1,2}$ and $c_{1,2}$ are integration constants and have to be determined by the requirements of continuity and differentiability of \dot{p} at $x = a$ and $x = b$ and the boundary conditions at $x = 0$ and $x = 1$. For the latter we choose $\dot{p} = 0$, which implies

$$a_2 = a_1 \quad \text{and} \quad (46)$$

$$c_2 = c_1 e^{2 \frac{p}{B_2 C}} \quad (47)$$

Together with the requirements of continuity and differentiability this yields the dispersion relation

$$\frac{\left(\frac{p}{B_1 C} + \frac{p}{B_2 C} \right) e^{\frac{p}{B_2 C} a} + \left(\frac{p}{B_1 C} + \frac{p}{B_2 C} \right) e^{\frac{p}{B_2 C} a}}{\left(\frac{p}{B_1 C} + \frac{p}{B_2 C} \right) e^{\frac{p}{B_2 C} a} + \left(\frac{p}{B_1 C} + \frac{p}{B_2 C} \right) e^{\frac{p}{B_2 C} a}} e^{2 \frac{p}{B_1 C} (a-b)} = \frac{\left(\frac{p}{B_1 C} + \frac{p}{B_2 C} \right) e^{\frac{p}{B_2 C} (b-1)} + \left(\frac{p}{B_1 C} + \frac{p}{B_2 C} \right) e^{\frac{p}{B_2 C} (b-1)}}{\left(\frac{p}{B_1 C} + \frac{p}{B_2 C} \right) e^{\frac{p}{B_2 C} (b-1)} + \left(\frac{p}{B_1 C} + \frac{p}{B_2 C} \right) e^{\frac{p}{B_2 C} (b-1)}} \quad (48)$$

Table 3. Eigenfrequencies (r : real part, i : imaginary part) of the three-zone model having the parameters $B_1 = 4$, $B_2 = \frac{1}{4}$, $a = 0.57$, $b = 0.59$, $\beta = 1$

r	12.01	16.78	18.55	24.86	25.83	31.29	34.67
i	0	0	0	0	0	0	0
r	0	0	0	0	0		
i	7.21	52.43	97.77	143.11	188.46		

where the eigenfrequencies are contained in the coefficient C . In general, the roots of equation 48 have to be calculated numerically, using, for example, a complex secant method. Separate spectra for the three isolated zones may be obtained by assuming the boundary conditions $\hat{p} = 0$ at $x = a; b$ instead of continuity and differentiability requirements. We are then left with the dispersion relations

$$D_{\text{inner}} = 1 = \frac{\left(\frac{p}{B_1 C} - \frac{p}{B_2 C} \right) e^{\frac{p}{B_2 C} a} + \left(\frac{p}{B_1 C} - \frac{p}{B_2 C} \right) e^{\frac{p}{B_2 C} a}}{\left(\frac{p}{B_1 C} + \frac{p}{B_2 C} \right) e^{\frac{p}{B_2 C} a} + \left(\frac{p}{B_1 C} + \frac{p}{B_2 C} \right) e^{\frac{p}{B_2 C} a}} \quad (49)$$

$$D_{\text{outer}} = 1 = \frac{\left(\frac{p}{B_1 C} - \frac{p}{B_2 C} \right) e^{\frac{p}{B_2 C} (b-1)} + \left(\frac{p}{B_1 C} + \frac{p}{B_2 C} \right) e^{\frac{p}{B_2 C} (b-1)}}{\left(\frac{p}{B_1 C} + \frac{p}{B_2 C} \right) e^{\frac{p}{B_2 C} (b-1)} + \left(\frac{p}{B_1 C} - \frac{p}{B_2 C} \right) e^{\frac{p}{B_2 C} (b-1)}} \quad (50)$$

$$D_{\text{shock}} = 1 = e^{2 \frac{p}{B_1 C} (a-b)} \quad (51)$$

for the inner, outer and shock zones, respectively.

For the averaged model we have $B_1 = 4$ and dominant radiation pressure implies $B_2 = \frac{1}{4}$. Inserting these values into equations 49-50 we are left with

$$q \frac{1}{\frac{1}{4} (4 + 3^2) a} = \frac{(2n+1)}{2} \quad n \geq 2 \quad (52)$$

$$q \frac{1}{\frac{1}{4} (4 + 3^2) (b-1)} = \frac{(2n+1)}{2} \quad n \geq 2 \quad (53)$$

Thus we have real, i.e., neutrally stable modes, if the inner and outer regions are considered separately, in accordance with the discussion in section 4.1.1. For the shock region equation 51 yields

$$2 \frac{p}{4^2 (4 + 3^2) (b-a)} = 2ni \quad n \geq 2 \quad (54)$$

These solutions correspond to purely imaginary implying instability. The solutions of equations 52-54 can be used as initial guesses for the numerical iteration of equation 48, the dispersion relation of the three-zone model. Some representative eigenvalues of the three-zone model are given in Table 3.

Once the eigenfrequencies are determined, the corresponding eigenfunctions are given by

$$p = \begin{cases} \sum_{n=0}^{\infty} a_n e^{\frac{p}{B_2 C} x} + a_2 e^{\frac{p}{B_2 C} x} & x \in [0; a] \\ b_1 e^{\frac{p}{B_1 C} x} + b_2 e^{\frac{p}{B_1 C} x} & x \in [a; b] \\ c_1 e^{\frac{p}{B_2 C} x} + c_2 e^{\frac{p}{B_2 C} x} & x \in [b; 1] \end{cases} \quad (55)$$

The factor e^x is due to the transformation from p to \hat{p} .

Typical eigenfunctions are presented in figures 6a1-6a3. Three types of modes may be distinguished belonging to the three zones of the model. Real eigenfrequencies are associated with the inner and outer region. "Shock modes" correspond to unstable and damped modes (purely imaginary pairs of eigenvalues). They oscillate in the shock region and are evanescent elsewhere. We note the correspondence of figures 6a1 and 4a1, 6a2 and 4a2 and 6a3 and 4a3, i.e., the results of the analytical model resemble those of the exact analysis. The influence of the shock position on the modal structure may also be studied within the framework of the three-zone model. As long as the width of the shock zone and the coefficient B_1 are not varied, the "shock modes" are not affected. The dependence on the shock position of the neutrally stable "inner" and "outer" modes is shown in figure 6b. Moving the shock position outwards, the frequencies of the inner modes decrease, whereas those of the outer modes increase, according to the variation of the length of the corresponding acoustic cavities. This leads inevitably to multiple crossings between the frequencies of the inner and outer modes, which unfold into avoided crossings (see, e.g., Gautschi & Glatzel (1990)). Mode interaction by instability bands is excluded here according to the general discussion in section 4.1.1.

4.1.3 Interpretation

The three-zone model reproduces the effects of the shock front regarding important aspects: The front acts as an acoustically isolating layer which separates the inner and outer part of the envelope. As a result, these parts provide largely independent

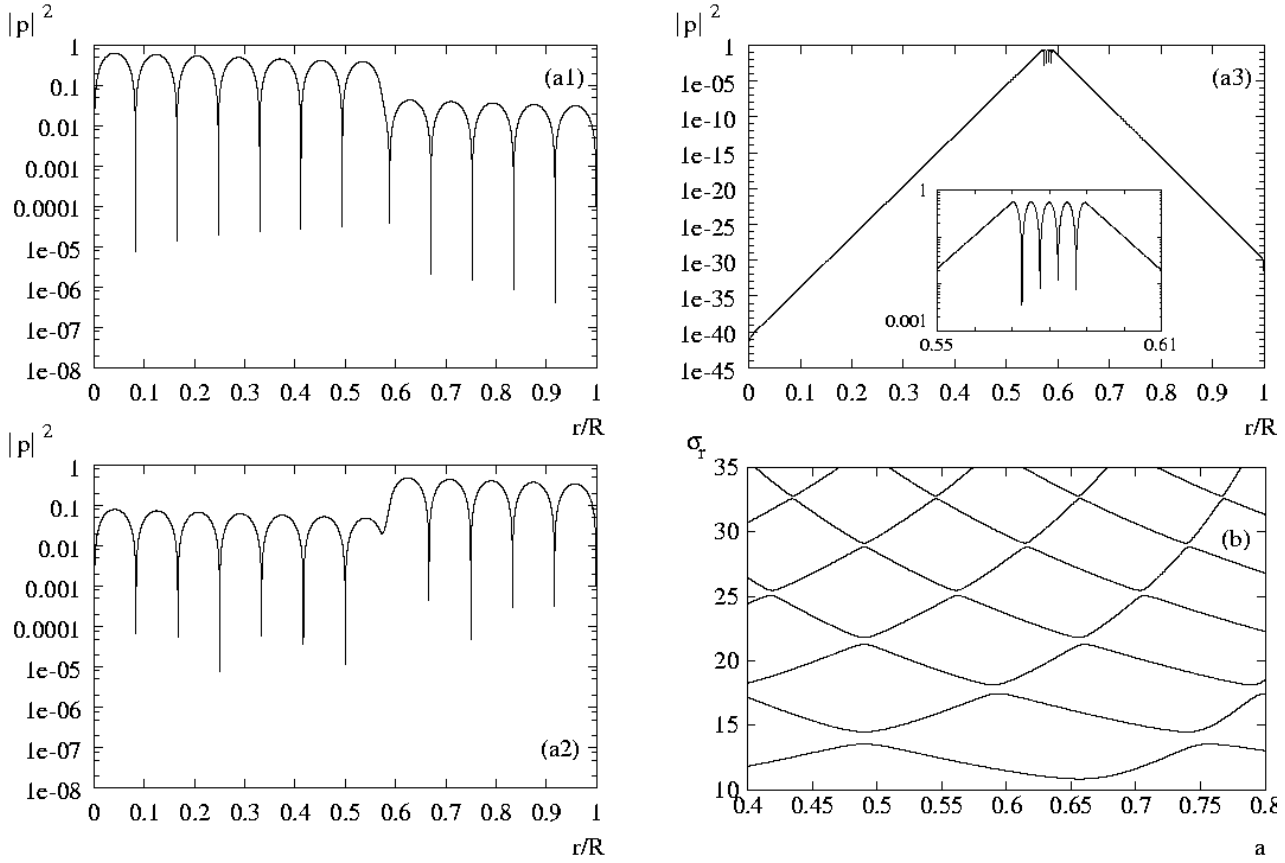


Figure 6. Eigenfunctions for the three-zone model with the parameters $B_1 = 4$, $B_2 = \frac{1}{4}$, $a = 0.57$, $b = 0.59$, $\gamma = 1$, and the frequencies $\omega_r = 44.04$, $\omega_i = 0$ (a1), $\omega_r = 43.53$, $\omega_i = 0$ (a2), $\omega_r = 0$, $\omega_i = 188.46$ (a3). (b): Eigenfrequencies ω_r of neutrally stable modes as a function of the position a of the lower boundary of the shock region for fixed $b = 0.02$ and $B_1 = 4$, $B_2 = \frac{1}{4}$, $\gamma = 1$.

spectra. This may be illustrated by the variation of the position of the shock front. Apart from the expected spectra associated with the inner and outer envelope, an additional spectrum of modes is generated by the shock region itself.

Comparing eigenfunctions of the averaged and the analytical model (figures 4a1-a3 and figures 6a1-a3), we find a strikingly similar behaviour. In particular, the content of the unstable shock modes is present in both cases. Due to constant coefficients, however, the analytical model reproduces neither decreasing amplitudes nor increasing spatial frequencies towards the stellar center.

We have identified unstable modes in the shock zone of the analytical model. They resemble those of the shock instabilities of the averaged model, and are related to the sound travel time across the shock zone. Its radial extent is primarily responsible for their high frequencies.

The analysis in section 4.1.1 has shown, that the sign of $u(x)$ in equation 38 is responsible for the instability in the shock region. This sign is determined by the term B_{\perp} , which is given by

$$\frac{B_1}{3} = \frac{1}{3} - \frac{\frac{p}{3}}{4 - \tau} \quad (56)$$

Estimating the various terms in equation 56, we find that the sign of p determines the sign of B_{\perp} . A dependence on the sign of p of the instability, however, is not recovered in the exact problem, which can be tested by replacing p with $-p$ there. The exact problem is not affected by this substitution. Thus we conclude, that the analytical model does not provide correct results in this respect and needs to be refined to describe the instability properly. In order to investigate the origin of the instability, some of the simplifying assumptions of the analytical model need to be dropped. In this direction, a more realistic model of the shock zone will be presented in the following section.

4.2 Shock-Zone-Model

Our study of the three-zone model in section 4.1 has shown, that inner, outer and shock zones may to good approximation be treated separately by assuming suitable boundary conditions, e.g., vanishing pressure at boundaries and interfaces. Moreover,

the instabilities of interest are not provided by the inner and outer zones. Therefore we restrict the following study to the shock zone by applying the boundary conditions $p(a) = p(b) = 0$. Within the framework of the analytical model the coefficients of the perturbation equations are taken to be constant with the values given in section 4.1.

Contrary to section 4.1 we will not replace the diffusion equation by an algebraic relation here, as this turned out to lead to erroneous results. However, we still adopt the NAR approximation. The set of equations considered then reads:

$$\frac{1}{dx} \frac{d}{dx} = \frac{1}{3} (3 + p - t) \quad (57)$$

$$\frac{1}{dx} \frac{dp}{dx} = (4 + 3^2) p \quad (58)$$

$$\frac{1}{dx} \frac{dt}{dx} = r (4 + p - t) \quad (59)$$

$$\frac{1}{dx} \frac{dl}{dx} = 0 \quad (60)$$

Written in matrix form this yields

$$\frac{1}{dx} \frac{d}{dx} \begin{pmatrix} p \\ t \\ l \end{pmatrix} = \begin{pmatrix} 1 & 0 & 1 \\ 0 & 1 & 0 \\ 0 & 0 & 0 \end{pmatrix} \begin{pmatrix} p \\ t \\ l \end{pmatrix} + \begin{pmatrix} 1 & 0 & 1 \\ 0 & 1 & 0 \\ 0 & 0 & 0 \end{pmatrix} \begin{pmatrix} p \\ t \\ l \end{pmatrix} \quad (61)$$

The differential equation is solved by an exponential dependence e^{ikx} of the dependent variables. Thus we arrive at the linear algebraic equation

$$\begin{pmatrix} 1 & 0 & 1 \\ 0 & 1 & 0 \\ 0 & 0 & 0 \end{pmatrix} \begin{pmatrix} p \\ t \\ l \end{pmatrix} + \begin{pmatrix} 1 & 0 & 1 \\ 0 & 1 & 0 \\ 0 & 0 & 0 \end{pmatrix} \begin{pmatrix} p \\ t \\ l \end{pmatrix} = \begin{pmatrix} 0 \\ 0 \\ 0 \end{pmatrix} \quad (62)$$

This equation has a non trivial solution only if the determinant of the matrix vanishes, which provides a quartic equation for the wavenumber k . One of its roots is zero, the remaining three roots are determined by the following cubic equation:

$$\frac{ik}{r(4-t)} + \frac{ik}{3} + \frac{ik}{(4-t)} \frac{1}{r(4-t)} (1 - \frac{1}{3}(4+3^2)) + \frac{1 + \frac{1}{3}(4+3^2)}{(4-t)} \frac{1}{3p(4+3^2) + \frac{4}{3}} = 0 \quad (63)$$

In the limit of large r they may be given in closed form:

$$\frac{ik}{1/2} = \frac{d_1}{2} \frac{r}{d_1^2} \quad (64)$$

$$\frac{ik}{3} = r(4-t) \quad (65)$$

The general solution to the perturbation problem consists of a superposition of four fundamental solutions associated with the four roots for the wavenumber, two of which are oscillatory (those associated with k_1 and k_2). The dispersion relation is then derived by imposing four conditions. In addition to the boundary conditions $p = 0$ at $x = a, b$, we require the two non oscillatory fundamental solutions not to contribute to the eigensolution. The latter is then only determined by k_1 and k_2 :

$$p = h_1 e^{ik_1 x} + h_2 e^{ik_2 x} \quad (66)$$

where h_1 and h_2 are integration constants. They are determined by the boundary conditions $p = 0$ at $x = a, b$, which imply

$$k_1 = k_2 = \frac{2n}{(a-b)} \quad (67)$$

where $n \in \mathbb{Z}$ denotes the order of the overtone. Using equation 64 we get

$$\frac{d_1^2}{4} = \frac{2n^2}{(a-b)^2} \quad (68)$$

With the definitions of d_1 and d_2 (equation 63) we arrive at a quadratic equation in k^2 . Expanding the coefficients of k^2 in

terms of $\frac{1}{r}$ and assuming $\frac{2n^2}{(a-b)^2}$ to be large, we obtain to lowest order in $\frac{1}{r}$:

$$4 \frac{\frac{9}{6}^2}{r^2 (4 - \tau)^2} - 2 \frac{p}{(4 - \tau)} + \frac{2n^2}{2(a-b)^2} = 0 \quad (69)$$

Defining

$$\tilde{r} = \frac{r^2 (4 - \tau)^2}{\frac{9}{6}^2} \quad (70)$$

this equation has the solutions

$$\frac{2}{1,2} = \frac{\tilde{r}}{2} \pm \frac{p}{(4 - \tau)} \pm \sqrt{\frac{\tilde{r}}{2} \pm \frac{p}{(4 - \tau)} + \frac{1}{\frac{4}{\tilde{r}^2 (a-b)^2} - \frac{1}{\frac{p}{(4 - \tau)^2}}} } \quad (71)$$

In the NAR-approximation, eigenfrequencies come in complex conjugate pairs, i.e., complex eigenfrequencies imply instability. According to equation 71, complex eigenfrequencies, and therefore instability, are obtained, if r is finite and n is sufficiently large. For fixed n we obtain in the limit of large r (expansion of the root):

$$\frac{2}{1} = \frac{1}{4} \frac{2n^2}{(a-b)^2} \frac{1}{\frac{p}{(4 - \tau)}} \quad (72)$$

$$\frac{2}{2} = \tilde{r} \pm \frac{p}{(4 - \tau)} \pm \frac{2}{2} \frac{2n^2}{(a-b)^2} \frac{1}{\frac{p}{(4 - \tau)}} \quad (73)$$

Equation 72 describes the eigenfrequencies of the decoupled shock modes discussed in section 4.1, i.e., the second order analysis of the previous section is contained in the limit $r \rightarrow 1$ of the present approach. Instabilities described by equation 71 resemble those of the averaged model, rather than those given by equation 72 for positive values of p . We conclude that a finite but large value of the stratification parameter $r = \frac{d \log T}{d \log p}$ is essential for instability. However, assuming $r \rightarrow 1$, which was done in the investigation of the three-zone model (section 4.1), is an oversimplification.

5 CONCLUSIONS

When following the non linear evolution of strange mode instabilities in the envelopes of massive stars, shock fronts were observed to be captured in the H-ionisation zone some pulsation periods after reaching the non linear regime. This effect is not observed in models of very hot envelopes (such as the massive star model investigated by Glatzel, Kiriakidis, Chemigovskij & Fricke (1999)), due to hydrogen being ionised completely. The shocks trapped in the H-ionisation zone perform high frequency oscillations (associated with the sound travel times across the shock zone) confined to its very vicinity, whereas the remaining parts of the envelope vary on the dynamical timescale of the primary, strange mode instability. By performing an appropriate linear stability analysis the high frequency oscillations were shown to be due to a physical instability, rather than being a numerical artifact.

An analytical model for the secondary, shock zone instabilities has been constructed. As a result, high values of r were found to be responsible for instability. Contrary to the common stratification (convective, Rayleigh-Taylor) instabilities driven by buoyancy forces and thus associated with (non radial) gravity modes, however, the instabilities found here are associated with spherically symmetric acoustic waves. An extension of the stability analysis to non radial perturbations would be instructive, since we expect the acoustic instabilities identified here – similar to strange mode instabilities (see Glatzel & Mehren (1996)) – not to be restricted to spherical geometry. Such an investigation would also reveal buoyancy driven instabilities, which we believe not to be relevant for the following reasons: Their typical timescale is much longer than that of the acoustic instabilities, which will therefore dominate the dynamics. Moreover, in addition to gravity, the acceleration due to the shock's velocity field has to be taken into account and is likely to stabilize the stratification with respect to convective instabilities. With respect to the aim of this paper to identify the secondary, shock oscillations and their origin, a non radial analysis is beyond the scope of the present investigation and will be the subject of a forthcoming publication.

Since the oscillations are a physical phenomenon – rather than a numerical artifact – they should not be damped by increasing the artificial viscosity as one would neglect a physical process whose influence on the long term behaviour of the system cannot yet be predicted. On the other hand, following the shock oscillations by numerical simulation for more than a few dynamical timescales is not feasible due to the small time steps necessary to resolve them. The confinement of the oscillations to the very vicinity of hydrogen ionisation, however, indicates a solution of the problem by means of domain decomposition: The stellar envelope is decomposed into three domains: below, around and above the shock. Only the narrow shock region needs high time resolution, the inner and outer zones merely require the dynamical timescale to be resolved. The development of a code following this strategy is in progress.

Even if the appearance of the shock oscillations has so far prevented us from performing simulations in excess of several dynamical timescales, the velocity amplitudes reach a significant fraction of the escape velocity. This indicates that pulsationally driven mass loss may be found in appropriate simulations. Whether the new code will allow for the corresponding long term simulations and thus possibly for the determination of mass loss rates, remains to be seen. Preliminary results will be published in a forthcoming paper.

ACKNOWLEDGMENTS

We thank Professor K. J. Fricke for encouragement and support. Financial support by the Graduiertenkolleg "Stromungsinstabilitäten und Turbulenz" (MG) and by the DFG under grant WA 633/2-1 (SC) is gratefully acknowledged. The numerical computations have been carried out using the facilities of the GWDG at Göttingen.

REFERENCES

- Baker N. H., Kippenhahn R., 1962, *Z. Astrophysik*, 54, 114
 Buchler J. R., Wahlen P., 1990, in *The Numerical Modelling of Nonlinear Stellar Pulsations Problems and Prospects*, ed. J. R. Buchler, NATO ASI Ser. C 302, Kluwer Academic Publishers, Dordrecht, 315
 Christy R. F., 1966, in Stein R. F., Cameron A. G. W., ed., *Stellar Evolution*. Plenum Press, New York, p. 359
 Cox J. P., 1980, *Theory of Stellar Pulsation*. Princeton Univ. Press, Princeton, NJ
 Dor E. A., Gautschy A., 2000, *ApJ*, 545, 982
 Fraley, G. S., 1968, *Ap&SS*, 2, 96
 Gautschy A., Glatzel W., 1990, *MNRAS*, 245, 154
 Glatzel W., 1994, *MNRAS*, 271, 66
 Glatzel W., Kiriakidis M., 1993, *MNRAS*, 263, 375
 Glatzel W., Kiriakidis M., Chemigovskij S., Fricke K. J., 1999, *MNRAS*, 303, 116
 Glatzel W., Mehren S., 1996, *MNRAS*, 282, 1470
 Humphreys R. M., Davidson K., 1979, *ApJ*, 232, 409
 Iglesias C. A., Rogers F. J., Wilson B. G., 1992, *ApJ*, 397, 717
 Kiriakidis M., Fricke K. J., Glatzel W., 1993, *MNRAS*, 264, 50
 Rogers F. J., Iglesias C. A., 1992, *ApJS*, 79, 507
 Samarskii A., Popov Yu., 1969, *Zh. Vychisl. Mat. i Mat. Fiz.*, 9, 953
 Schamuter W. M., Winkler K.-H., 1979, *Comp. Phys. Comm.*, 18, 171
 Unno W., Osaki Y., Ando H., Saio H., Shibahashi H., 1989, *Nonradial Pulsations*. Univ. Tokyo Press, Tokyo

This paper has been typeset from a \LaTeX / \LaTeX file prepared by the author.